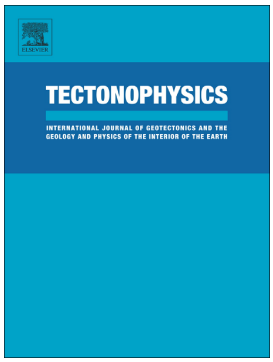


# Patagonian landscape modeling during Miocene to Present-day slab window formation

Pilar Ávila, Milagros Ávila, Federico M. Dávila, Miguel Ezpeleta, Nesvit E. Castellano

PII: S0040-1951(23)00269-X

DOI: https://doi.org/10.1016/j.tecto.2023.229971

Reference: TECTO 229971

To appear in: *Tectonophysics*

Received date: 1 September 2022

Revised date: 16 June 2023

Accepted date: 19 June 2023

Please cite this article as: P. Ávila, M. Ávila, F.M. Dávila, et al., Patagonian landscape modeling during Miocene to Present-day slab window formation, *Tectonophysics* (2023), https://doi.org/10.1016/j.tecto.2023.229971

# Patagonian landscape modeling during Miocene to Present-day slab window formation

Pilar Ávila[1], Milagros Ávila[2], Federico M. Dávila[1], Miguel Ezpeleta[1] and Nesvit E. Castellano[2]

[1]CICTERRA, CONICET - Facultad de Ciencias Exactas, Físicas y Naturales, Universidad Nacional de Córdoba, Córdoba 5016, Argentina.

[2] Facultad de Matemática, Astronomía y Física, Universidad Nacional de Córdoba, Córdoba 5016, Argentina.

Corresponding author: p.avila@unc.edu.ar



## ABSTRACT

The subduction of seismic oceanic ridges often results in the formation of slab windows, which can affect not only the heat flow and retroarc volcanism, but also the exhumation and topographic evolution of the upper plate. An active and world-class example of a slab window is southern Patagonia, in southernmost South America, which is related to the subduction of the seismic oceanic South Chile Ridge between the middle–late Miocene and the Present day. How the subduction of the ridge and formation of the slab window have influenced the evolution of the Patagonian landscape, exhumation and topography is still under debate. Some works have proposed orogenic deformation mostly affecting the Pacific margin and hinterland areas, or an inherited early Miocene tectonic relief generated before the slab window formation. Others have preferred epeirogenesis hypotheses, such as dynamic uplift or isostatic rebound as a result of lithospheric thinning associated with asthenospheric or lithospheric mantle changes. In this work, we analyze the landscape evolution at medium (orogen-scale) and long

wavelengths (embracing the whole of southern Patagonia, from coast to coast) using FastScape a landscape numerical model. This program was coupled with an optimization scheme (the Neighborhood Algorithm) suitable for nonlinear inverse problems. The "goodness" (fit to data) of our landscape evolution models was evaluated using: i) cooling ages, and ii) maximum elevations, in order to provide constraints on the uplift rates, erosion efficiency and effective elastic thickness. We then used the best values to compare two forward models representing medium- versus long-wavelength processes. Our results indicate that long-wavelength uplift geometry (including dynamic uplift and/or lithospheric rebound from thinning) involving areas from the Andes to the Atlantic coast was required from 12 Myr to the Present day in order to reproduce not only the youngest cooling ages but also Present-day topography.

**Keywords:** Slab window; Southern Patagonia; Inverse modeling; Isostatic rebound

## 1. Introduction

The subduction of seismic oceanic ridges and formation of asthenospheric or slab windows are genetically related processes that strongly affect and modify the configuration and evolution of overriding plates (Thorkelson, 1996; Thorkelson et al., 2011). Regions overlying these geological windows are characterized by high heat flows (Ávila and Dávila, 2018; Groome and Thorkelson, 2009), back-arc alkaline magmatism (Aragón et al., 2013; Gorring et al., 1997), deformation and seismicity focused along the margin and forearcs (e.g., Georgieva et al., 2016), low intra-lithospheric seismic velocities (Russo et al., 2010; Suárez et al., 2021), thickness reduction of the lithospheric mantle (Ávila and Dávila, 2020; Curie and Hyndman, 2006), and formation of topographic plateaus (Ávila and Dávila, 2020; Guillaume et al., 2009; Thorkelson et al., 2011). The most studied active examples are in the North America Cordillera, Central America and southern Patagonia (see Thorkelson et al., 2011). Ancient slab windows

have also been reported in the southern/central Andes (Aragón et al., 2013; Gianni et al., 2018; Martina et al., 2020), Japan (Underwood, 1993), and Alaska (Haeussler et al., 2003).

The modern southern Patagonia case is associated with the subduction dynamics of the seismic oceanic South Chile Ridge (Breitsprecher and Thorkelson, 2009; Ramos and Kay, 1992). In this region, although there is a relative consensus on the connections between the magmatic evolution and the formation of a slab window, the processes involving the thermal states and uplift across Patagonia are still strongly discussed (see Ávila and Dávila, 2020, 2018; Christeleit et al., 2017; Georgieva et al., 2019, 2016; Guillaume et al., 2013, 2009; Husson et al., 2019; Stevens Goddard and Fosdick, 2019; Thomson et al., 2010; and Willett et al., 2020).

The Cordilleran belt has shown little or no crustal shortening from the late Miocene to the Present day (Ghiglione et al., 2016), which correlates with the formation stage of the slab window. Structural sections showed that for the last 12 Myr, extensive plateau basalts with geochemical signatures of asthenospheric mantle (Gorring et al., 1997; Guivel et al., 2006; Lagabrielle et al., 2007) rest on the eastern thrust front of the Southern Patagonian Andes (Ghiglione et al., 2016; Lagabrielle et al., 2007). These observations suggest that the main shortening (roughly orthogonal to the Andean belt) would have ceased before the arrival of the South Chile Ridge (Guillaume et al., 2009; Lagabrielle et al., 2007; Scalabrino et al., 2010). Nevertheless, an increase in both summit elevations and local relief, as well as an important exhumation event, have been described along the southernmost Patagonian Andes during the last 10 Myr (Georgieva et al., 2016; Thomson et al., 2010). In addition, towards the distal foreland and passive Atlantic margin, a moderate elevation plateau (500–1000 m asl) has developed since the late Miocene (Guillaume et al., 2009; Pedoja et al., 2011). Some works have proposed that the oceanic ridge collision drove a deformation stage, mostly along the Pacific margin and hinterland (Georgieva et al., 2016; Stevens Goddard and Fosdick, 2019). Others have suggested an inherited tectonic relief generated before the slab window formation

(Andrić-Tomašević et al., 2021; Colwyn et al. 2019). Regional dynamic uplift (including the foreland to Atlantic margin areas) caused by the cessation of dynamic deflection generated by the Nazca plate (Guillaume et al., 2009) or isostatic rebound by reduction of lithospheric thickness (Ávila and Dávila, 2020) have also been proposed.

The aim of this paper is to provide new insights into the main driving forces that could have generated topographic changes since the arrival of the asthenospheric window in southern Patagonia. To address this issue, we analyzed the landscape evolution at medium (orogen-scale) and long wavelengths (embracing the entire breadth of Patagonia, from coast to coast) using FastScape, a landscape numerical model (Braun and Willett, 2013).

## 2. Geological and geodynamic setting

The study region comprises southernmost South America, between the Southern Andean Cordillera to the west, and the passive Atlantic platform to the east (45° and 55° S, Fig. 1a). These regions are bounded to the west by the Nazca and Antarctic oceanic plates, intersecting the Chile trench at ~46.5° S" (Fig. 1a). The Nazca slab, to the north, plunges to the east with a dip of around 30–45° with a convergence velocity of 7 cm/yr, and extends at least until the 670-km mantle discontinuity, whereas the Antarctic plate, to the south, displaces at 2 cm/yr, is sub-horizontal and only subducts for ~100 km from the trench (Breitsprecher and Thorkelson, 2009; Suárez et al., 2021). The junction of these three plates (Nazca, Antarctica and South America) defines the Chile Triple Junction (CTJ) (Fig. 1a). The oceanic South Chile Ridge (and CTJ) would have migrated from ~55˚–54° S northward for ~1000 km, from 16 Myr (Middle Miocene) to the Present day. These plate kinematics have been associated with the formation of an asthenospheric or slab window (Fig. 1a, Breitsprecher and Thorkelson, 2009; Ramos and Kay, 1992). The occurrence of a volcanic arc gap since the middle–late Miocene (e.g. Suárez et al., 2021), alkaline volcanism in the back-arc from ~12 Myr (e.g. Gorring et al.,

1997; Guivel et al., 2006; Ramos and Kay, 1992), low-velocity zones in seismic tomography (Mark et al. 2022; Russo et al., 2010; Suárez et al., 2021), high heat flows (Ávila and Dávila, 2018), rapid exhumation in the last ~10 Myr (Guillaume et al., 2009; Stevens Goddard and Fosdick, 2019), and anomalous elevations across the foreland (Ávila and Dávila, 2020) have supported this interpretation.

*2.1 Topography, uplift and exhumation*

Northward of the CTJ, overlying the Nazca plate subduction zone, the elevations along the Cordilleran axis are <2300 m asl. In contrast, south of the CTJ, overlying the slab window and Antarctic subduction zone, the altitudes are >3000 m asl (maximum elevations are around 3200 m asl, Fig. 1a). These regions have been affected by moderate-to-no crustal shortening across the hinterland during the last 12 Myr (Kreitsprecher and Thorkelson, 2009; Lagabrielle et al., 2007; Scalabrino et al., 2010), whereas the forearc deformation was mainly driven by transpression associated with the Liquiñe-Ofqui strike-slip fault zone (Georgieva et al., 2016; Suárez et al., 2021). Towards the distal foreland and passive Atlantic margin, Patagonia developed a moderate elevation plateau (500–1000 m asl, Fig. 1b) (Guillaume et al., 2009; Lagabrielle et al., 2007; Pedoja et al., 2011) which exposes undeformed and flat-lying Upper Oligocene–Lower Miocene marine strata and Upper Miocene basalts (see Ávila and Dávila, 2020). In this region, similar to observations in the Cordilleran sections, no major crustal tectonic structures seem to explain the uplift history and plateau formation (see Ávila and Dávila, 2020).

Low-temperature thermochronology studies and exhumation modeling using different thermochronological systems (from apatite fission track, AFT, to apatite helium, AHe) along the Cordillera showed a variety of ages from Cretaceous to Pliocene (Andrić-Tomašević et al., 2021; Georgieva et al., 2019, 2016; Guillaume et al., 2013; Haschke et al., 2006; Stevens

Goddard and Fosdick, 2019; Thomson et al., 2010). However, the cooling ages using the lowest closure temperatures (AFT and AHe) reported values <10 Myr (see Andrić-Tomašević et al., 2021). Considering that the region has had poor (and possibly no) tectonic shortening since the late Miocene, this period of cooling has been related to high erosion (Miocene to Pleistocene glaciations), inherited topography, high geothermal gradients, or relief formation by epeirogenic processes (Andrić-Tomašević et al., 2021; Colwyn et al., 2019; Guillaume et al., 2013; Stevens Goddard and Fosdick, 2019; Thomson et al., 2010). It is important to emphasize that from 12 Ma, southern Patagonia was affected by the combined effects of two major mechanisms, from the surface to deep Earth: (1) The late Neogene glaciations (6–7 Ma, Coronato and Rabassa, 2011; Herman and Brandon, 2015; Mercer and Sutter, 1982), and (2) the formation of a slab window (Ávila and Dávila, 2018; 2020; Guillaume et al., 2009). Haschke et al. (2006) and Guillaume et al. (2013) analyzed AFT data at local and larger scales between 45°S and 48°S, respectively, and concluded that the slab window drove a reheating phase between 15 and 6 Ma, before the major cooling or exhumation stage. However, more recently, Georgieva et al. (2019) and Stevens Goddard and Fosdick (2019) analyzed a larger database and far more model inversions, and proposed continuous cooling since the early Cenozoic, instead of this heating event.

This elevation data and the lack of crustal shortening across the Andes, foreland and Atlantic margin, together with the high exhumation rates reported along the Cordilleran belt since the Late Miocene, have led some authors to propose different hypotheses to explain the uplift history. Georgieva et al., (2016) associated different structural observations and thermochronological data with short-wavelength processes. They proposed a stepwise exhumation for the last 10 Myr driven by glacial erosion that affected a complex structural mosaic, dominated by transpressional tectonics, likely related to the South Chile Ridgesubduction. On the other hand, Stevens Goddard and Fosdick (2019) based their

hypothesis on the Furlong and Govers (1999) model, and proposed the generation of a thickened ridge-parallel crustal welt, which preceded the arrival of the subducting ridge, affecting an area of >160 km from the trench to the foreland. Other studies have tested the epeirogenesis hypotheses associated with thermal evolution linked to the oceanic ridge subduction and formation of the Patagonian slab window (e.g., Guillaume et al., 2009). While Guillaume et al. (2013) inclined towards a positive change of dynamic topography or a dynamic uplift component to account for both topography and thermochronological data, Ávila and Dávila (2020) proposed an isostatic rebound by lithospheric thinning driven by heat flow increase (Ávila and Dávila, 2018).

*2.2 Paleotopography and Neogene stratigraphy*

A key point for our topographic analysis is to define the scenario from which the model starts. For most authors, the widespread distribution of shallow marine beds in Patagonia (Centinela Fm. and correlatives, see Cuitiño et al., 2016, 2012; Parras and Cuitiño, 2021 among others, Fig. 1a) suggests that the study region was below, or close to, sea level in the late Oligocene–early Miocene (i.e., prior to slab window formation). These strata are unconformably followed by upward-coarsening alluvial synorogenic beds (Santa Cruz Fm., and correlatives; Cuitiño et al., 2016; 2012), interpreted as the main phase of Cenozoic deformation and surface uplift in the Patagonian Cordillera (Blisniuk et al., 2005; Lagabrielle et al., 2007). The southern Patagonia foreland would have been characterized by a subtropical humid climate in the Paleogene to middle Miocene, and a semiarid to arid climate since then (Blisniuk et al., 2005; Flynn and Swisher, 1995; Pascual and Jaureguizar, 1990). In consistency with this, and based on carbon and oxygen isotope analyses of pedogenic carbonate nodules from this unit, Blisniuk et al. (2005) interpreted an increase in aridity across the eastern foreland, and attributed it to the formation of an orographic rain shadow by the middle Miocene

(*ca.* 16.5 Ma). By ~12 Myr the synorogenic deposition across the foreland ended (Ghiglione et al., 2016), and Mio-Pliocene to Pleistocene glacial tillites and recurrent basalt layers developed, overlying the upper Miocene Santa Cruz Formation (Coronato and Rabassa, 2011; Mercer and Sutter, 1982; Rabassa and Coronato, 2002). These are undeformed, flat lying, and, as mentioned above, indicate the end of deformation, foreland uplift, and the contemporaneity of glacial and mafic volcanic activity (Lagabrielle et al.; 2007). On the other hand, Colwyn et al. (2019) used water isotopes in hydrated volcanic glass to interpret the Patagonian topography through time. In contrast to the widely held view that the Patagonian Andes formed during the Miocene and that the area was under or close to sea level during the Late Oligocene to Early Miocene, these authors proposed that the topography began to grow continuously without interruptions from the Late Cretaceous. Their results suggest that a significant isotopic rain shadow, of a magnitude similar to the modern one, would have existed in Patagonia since at least the Paleocene. Based on these results they proposed a main Cretaceous uplift and the creation of a high topography between 135 Myr and 70 Myr, followed by relative stability throughout the Cenozoic to the Present day. They also suggested that marine sedimentation during the Late Oligocene-Early Miocene would have been localized incursions.

## 3. Landscape evolution model

We used FastScape, a landscape numerical model (Braun and Willett, 2013), to explore the evolution of the Patagonian landscape since the arrival of the slab window, from the middle–late Miocene to the Present day. Our main target was to analyze the long- and medium-wavelength topographic evolution to the south of the CTJ, between the Pacific and Atlantic coasts, as well as the low-temperature thermochronology reported along the Patagonian Cordillera since the last and most rapid exhumation episode (<12 Ma; Stevens Goddard and Fosdick, 2019). Figure 2 summarizes the models and scenarios analyzed in this study. We

tested two competing hypotheses or models (Models 1 and 2), considering two likely initial topographic scenarios (*a* and *b*) in each model. Scenario *a* considers a flat initial topography, assuming the region was below sea level in the Late Oligocene to Early Miocene, as widely proposed (see above). Scenario *b* follows the Colwyn et al. (2019) proposal of an initial topography similar to the Present day across the Cordillera. In Model 1 (scenarios *a* and *b*), the topography and low-temperature rock cooling were fully controlled by medium-wavelength (orogen-scales, >300 km) processes affecting the orogenic width, as suggested by Georgieva et al. (2016, 2019), Stevens Goddard and Fosdick (2019), and Andric-Tomasevic et al. (2021). In Model 2 (scenarios *a* and *b*), rock cooling and topography were mainly driven by long-wavelength processes (<300 km), such as dynamic uplift (Guillaume et al., 2009) or isostatic rebound (Ávila and Dávila, 2020).

### *3.1 Direct model: FastScape*

FastScape (Braun and Willett, 2013) includes an unconditionally stable implicit solution to the stream power equation:

$$e = \frac{\partial h}{\partial t} = U - KA^m S^n = U - KA^m \left(\frac{\partial h}{\partial x}\right)^n \quad (1)$$

where e is the rate of topographic change; h is topographic height; t is time; U is the assumed rock uplift function; S (dh/dx) is the local slope; and A is the drainage area (see Whipple and Tucker, 1999). Parameters k, m, and n are constants that mostly depend on lithology and climate; m is the discharge exponent fixed at 0.4, n is 1, and k is an erodibility factor that depends mainly on lithology and channel width (for further details see Croissant and Braun, 2014; Whipple and Tucker, 1999).

The erosion rates in fluvial and glacial erosion processes are primarily controlled by the slope and geometry of first order drainage systems. Nevertheless, the stream power law and a simple diffusion-like representation of hillslope processes may not be the best solution for modeling glaciated landscapes. However, to date, the algorithms that solve the glacial erosion equations (e.g., Braun et al., 1999; Hergarten, 2021) require glacial parameters that are difficult to define. In addition, these solutions are not efficient enough, particularly for running inversions like those carried out in this work.

*3.1.1 Parameterization*

The models were performed on a rectangular domain of 800×700 km (Fig. 2), discretized by 1×1 km regular space nodes. This space represents the dimensions of southern Patagonia (Fig. 1a). All models run for 20 Myr. The time step length was fixed to 1 kyr. For Model 1*a* and 2*a*, initial topography (at 20 Ma) was set as flat and near sea level in order to simulate the marine stratigraphic descriptions and paleotopography interpretations during the late Oligocene–early Miocene (see geological setting above). For these models the precipitation rates were introduced as functions that change in space and time (Fig. 2). For the first 3.5 Myr (i.e., from 20 to 16.5 Ma), the model ran at a homogeneous rate of 1500 mm/yr across the domain in order to simulate humid climates (cf. Blisniuk et al., 2005; Flynn and Swisher, 1995; Pascual and Jaureguizar, 1990). After 3.5 Myr (i.e., from 16.5 to 0 Ma), according to the orographic barrier model of Blisniuk et al. (2005), the precipitation rates were 3000 mm/yr to the west of the Cordillera and 200 mm/yr to the east (Gaussian function that simulates an orographic barrier), particularly along the Patagonian foreland (see Fig. 2). For Models 1*b* and 2*b*, the initial topography was set as similar to the Present-day Cordillera and flat across the foreland to the coastal region, close to sea level (cf. Colwyn et al., 2019 hypothesis) in order to guarantee the marine incursions during the late Oligocene to early

Miocene (Fig. 2). This topography is represented by two gradients in a vertical displacement along a north–south boundary. From the left boundary to 100 km, the topography increases linearly until 3200 m asl (maximum height). From 100 km to 150 km (towards the right), the topography decreases linearly to 0 m (Fig. 2). This initial geometry allows those areas where marine strata accumulated to be explained. For these latter models, precipitation rate was introduced as a Gaussian function that simulates an orographic barrier; the precipitation rate was 3000 mm/yr to the west of the Cordillera and 200 mm/yr to the east (see Fig. 2).

*3.1.2 Uplift rate functions and flexural isostasy*

Uplift functions were used in combination with flexural isostasy functions that reproduce the lithospheric unloading caused by erosion. Fastscape incorporated the flexural equation using a thin elastic plate model (Braun and Willett, 2013). To account for the isostatic rebound, FastScape solves the bi-harmonic flexural equation for a thin elastic plate subject to surface loading/unloading:

$$D\frac{d^4w}{dx^4} + D\frac{d^4w}{dy^4} + D\frac{d^4w}{dz^4} = \Delta\rho g w + \rho_c g \Delta h \qquad (2)$$

where w is the surface displacement associated with the isostatic adjustment of an increment in erosion Δh; Δρ is the density contrast between asthenospheric density (ρa=3300 kg/m3) and surface rock density (ρs=2800 kg/m3); $D = \frac{ET_e^3}{12(1-\nu^2)}$ is flexural rigidity, where E is Young's modulus (70 x $10^9$ Pa), ν is Poisson's ratio (0.25), and Te is effective elastic thickness (Turcotte and Schubert, 2002). All these parameters are constant in space and time.

The first geodynamic hypothesis tested in this work (Models 1*a* and *b*) starts with an uplift rate $U_{t1}$ (Fig. 2b) that simulates the crustal tectonic shortening and deformation along the

Cordillera described in different structural studies (e.g., Aramendía et al., 2022; Fosdick et al., 2013; Ghiglione et al., 2016). $U_{t1}$ allowed the reproduction of the main phase of early–middle Miocene deformation and related surface uplift that occurred in the Patagonian Andes during the early Neogene (cf. Lagabrielle et al., 2007; Blisniuk et al., 2005, see Fig. 1a). This can be illustrated as a tectonic wedge, represented by two gradients in a vertical displacement rate along a north–south boundary. From the left boundary to 200 km, the uplift rate increases until $U_{t1}$ (maximum uplift rate). From 200 to 260 km (right boundary), the uplift rate decreases linearly to 0 mm/yr (Fig. 2b). Although the function $U_{t1}$ is simple for modeling the orogenic growth as a consequence of tectonic shortening, it satisfies the magnitudes and geometry to account for the tectonic and paleoclimatic scenarios mentioned above. Models 1*a* and 1*b* assume that the reliefs continued to be influenced by crustal deformation along the 260 km-wide Andean belt described above, associated with tectonic shortening after the arrival of the South Chile Ridge (Fig. 2). The rock uplift rate function ($U_{t1}$) ceases as the ridge subduction migrates northward, i.e., the uplift is being canceled (backwards) as the ridge moves forward (Fig. 2) at a constant velocity (8 mm/yr).

The second geodynamic hypothesis tested in this work (Models 2*a* and *b*, Fig. 2) starts with the same geometry for the uplift rate $U_{t1}$ as Model 1. In these models, the rock uplift rate function $U_{t2}$ runs for *ca*. 8 Myr (i.e., from 20 until 12 Ma, the age of the oldest and undeformed basalt). $U_{t2}$ was imposed (not inverted, as in Model 1) with values of 2 mm/yr. Once the function $U_{t2}$ ends at 12 Ma, the uplift rates change to $U_m$ in order to simulate the influence of a subcrustal-driven or long-wavelength uplift. To simulate this rock uplift rate, we developed a Gaussian-type function $U_m$. The function $U_m$ affects the entire domain width (from W–E) of southern Patagonia, from the Pacific coast to the Atlantic margin (Fig. 2). The function describes a pulse that migrates in time at a constant velocity (8 mm/yr). This migration coincides with the advance of the Chile Ridge to the north. σ2 is 150 km to guarantee that the

area affected by the function is similar to the one proposed by Guillaume et al. (2009). Considering that the sublithospheric processes associated with the asthenospheric window should be higher near the trench, where the thermal anomalies are higher, the Um function decreases linearly from west to east with a slope of 0.8 (Ávila and Dávila, 2020).

*3.2 Inverse Model: Neighborhood Algorithm (NA)*

For our computations, we used Fastscape coupled with an optimization scheme suitable for non-linear inverse problems (Neighborhood Algorithm, NA; Sambridge, 1999). We defined the "goodness" (fit to data) using: i) cooling ages younger than 10 Ma, and ii) maximum elevations at the Present day. To perform this inversion model, we used 92 thermochronological samples (AHe and AFT) from Patagonia (see location in Fig. 1a, compiled from Blisniuk et al., 2005; Christeleit et al., 2017; Georgieva et al., 2016; Guillaume et al., 2013; Haschke et al., 2006; Thomson et al., 2001; 2010; and Willet et al., 2020). Ages older than 10 Myr were discarded since they reflect the cooling histories prior to the arrival of the Chile Ridge in southern Patagonia. We also used the maximum elevation along the Andean belt (3200 m asl) and Patagonian foreland (800 m asl) to perform the inversion. These data were extracted from a swath profile (generated with a DEM STRM 90 m) of the study region considering a width (south–north) similar to the model extension (Fig. 1b). These profiles were also used to compare models with observed topography.

The NA (Sambridge, 1999) is a search method that finds acceptable data fit models in a multidimensional parameter space. Rather than looking for a single optimal model, the NA finds a set of models that preferentially shows the good data-fitting regions of the parameter space. This algorithm uses the geometric constructions of Voronoi cells to generate the search in the parameter space. These are the closest neighborhood regions defined under a suitable distance rule. The algorithm is conceptually simple, requires only two "fitting parameters", and

uses a range of data rather than a defined numeric value. In this way, all the difficulties associated with scaling a data fit function are avoided, and any combination of data fit criteria can be used.

As stated above, we tested our models by comparing the predicted against the measured (or observed) low-temperature thermochronology and maximum elevation from the Pacific to the Atlantic coast (see Fig 1b). FastScape can reproduce cooling ages at specific locations for different thermochronometers – Apatite and zircon fission tracks (AFT and ZFT), and apatite and zircon helium (AHe and ZHe). The program solves the heat conduction/advection/production equation in 1D to obtain thermal histories:

$$k\frac{\partial^2 T}{\partial z^2} = v\frac{\partial T}{\partial t} + \frac{\partial T}{\partial z} \quad (3)$$

where κ is thermal diffusivity and v is the erosion rate predicted by FastScape. We assume that the top and base of the crust are held at a constant temperature: $T_{z=0}$ = 0°C, $T_{z=L}$ = 800 °C and L = 30 km. We also tested two end members for Tz=L = 600 and 1000°C (see Supplementary Material Fig. S1). These thermal histories are then used to obtain ages by solving the Fission Track annealing equation and the solid state He diffusion equation (Braun et al., 2006).

The parameters constrained by the inversion of thermochronological ages and present-day topography were the erosion efficiency (k), rock uplift rate ($U_{t1}$ and $U_m$), and effective elastic thickness (Te). The chi-square ($\chi 2$) goodness of fit function is used to quantify the discrepancy between the values modeled in FastScape and the observed geological data:

$$\chi 2 = \left(\frac{\left(H^{pred} - H^{obs}\right)^2}{{\sigma_{H_{obs}}}^2}\right) + \sum_{i=1}^{m} \left(\frac{\left(Age_i^{pred} - Age_i^{obs}\right)^2}{{\sigma_{Age_{obs}}}^2}\right)/m \quad (4)$$

where m is the number of thermochronological ages; $Age^{obsi}$ and $Age^{predi}$ are the observed and predicted ages; and $\sigma Age_i$ is the uncertainty on the observed ages. $H^{obs}$ and $H^{pred}$ are the observed (Present-day) and predicted maximum topography of Patagonia, and $\sigma H_{obs}$ is the regional variability (200 m). NA repeatedly uses these values to resample the parameter space in a way that leads to an optimal and effective search to minimize the fit function (Sambridge, 1999). For each geodynamic scenario, we ran 3000 models for the first iterations, and 4000 to explore the parameter space; we then performed 300 iterations with 150 resampled cells.

## 4. Results

Figures 3–6 show the results from the NA inversion (which define the best orogenic uplift $U_{t1}$ or $U_m$, effective elastic thickness Te, and erodibility parameters k) and forward computations to compare modeled and observed topography and thermochronology. The inversion models were illustrated with scatter plots as values of the misfit function for pairs of free parameters (Fig. 3a, 4a, 5a and 6a). In the panels, each dot represents a single FastScape model run. The color scale refers to the misfit value of the run; reds indicate the best fitting areas. In each of the panels, the red star indicates the position of the best-fitting model in the parameter space. In addition, we have illustrated a comparison between the modeled AHe and AFT ages, and maximum and mean topography for the best-fit model (lowest misfit) against the same observed (or measured) values. This allows us to make visual comparisons between the results of the two geological hypotheses (Models 1 and 2) and the two scenarios (*a* and *b*) described in the methodology and below. In the Supplementary Material, we show two end member results that consider different temperatures at the base of the crust (Fig. S1). These results show that AHe and AFT ages tend to be younger with lower basal temperature and older

with hotter basal temperature. This suggests that basal temperature has a minor influence on the models (note that the AHe and AFT ages are + - 1 Myr with respect to 800°C).

*4.1 Model 1a (Flat initial topography and uplift localized along the orogenic belt)*

The misfit for the best free parameters in the NA inversion model was 4.6 (Fig. 3a). The values for $U_{t1}$, Te and k were constrained between 1.7.0–2.5 mm/yr, 55–65 km and 1.5–4 x $10^{-5}$ $m^{1-2m-1}$, respectively (see Supplementary Material Fig. S2). In turn, the NA inversion results showed best fits (red star) 1.9 mm/yr for $U_{t1}$, 62 km for Te and 1.8 x $10^{-5}$ $m^{1-2m-1}$ for k. With these best fits, we ran a forward model using Fastscape. Figures 3b–d show these results, where we compared observed versus modeled thermochronological ages (Fig. 3b) and topography in N–S and W–E swath profiles (Figs. 3c and 3d). The thermochronological correlation (modeled versus observed) of both systems was, in general, acceptable, with a Mean Squared Error (MSE) of 5.6 (Fig. 3b). The topographic profiles correlate rather well. While the N–S maximum swath profile has a remarkable similarity, the W–E swath profile shows only a good correlation across the orogenic area in the Andes (first 400 km, from W to E). The correlation across the extra-Andean plateau, from 400 km eastward, is not good. Note that the modeled topography is close to sea level from across the foreland to the Atlantic margin (Fig. 3d), whereas the observed elevations are >500 m (Fig. 3d). However, the correlation was poor in both profiles (N–S and W–E) for the mean swaths (the modeled topography is lower than the observed topography).

*4.2 Model 1b (Initial topography with an orogenic relief and uplift localized along the orogenic belt)*

The misfit for the best free parameters was 4.7 (Fig. 4a). The values for $U_{t1}$, Te and k were constrained between 1.71–3.0 mm/yr for $U_{t1}$, 65–80 km for Te and 1–2.5 x $10^{-5}$ $m^{1-2m-1}$

for k (see Supplementary Material Fig. S3). In turn, the NA inversion results showed best fits (red star) of 2.7 mm/yr for $U_{t1}$, 78 km for Te and 2.02 x $10^{-5}$ $m^{1-2m-1}$ for k. These values are higher than the ones calculated for Model 1a. With these fitting values, we ran a forward model using Fastscape. Figure 4 shows these results, where we compared observed versus modeled thermochronological ages (Fig. 4b) and topography in N–S and W–E swath profiles (Figs. 4c and 4d). In general, the thermochronology correlation of both systems was acceptable, with an MSE of 5.8 (Fig. 4b). As in Model 1*a*, the topographic profiles depicted good correlations. The N–S maximum swath profile shows a remarkable correlation, whereas the W–E maximum swath profile has a good correlation across the orogenic area in the Andes (the first 250 km, from W to E), but correlates poorly across the extra-Andean plateau, from 400 km eastward. However, as in Model 1*a*, the correlation was poor in both profiles (N–S and W–E) for the mean swaths (the modeled topography is lower than the observed topography).

*4.3 Model 2a (Flat initial topography and long-wavelength uplift)*

The misfit for the best fitting three parameters was 4.2, suggesting that this model acceptably reproduces the maximum topography and thermochronology data (Fig. 5a). The $U_m$, k and Te were well constrained, with values of 0.2–1 mm/yr, 29–36 km and 0.2–0.5 x $10^{-4}$ $m^{1-2m-1}$, respectively (see Supplementary Material Fig. S4). In turn, the inversion results show that the observed data are best explained using 0.33 mm/yr, 35 km and 0.28 x $10^{-4}$$m^{1-2m-1}$ for $U_m$, Te and k, respectively. Figures 5b–d show these results and the relationships between observed and predicted thermochronological ages and maximum and mean topography across N–S and W–E swath profiles. In general, the thermochronology correlation of both systems was good, with an MSE of 3.6 (see Fig. 5b). The N–S modeled maximum swath profile matches observed peaks but does not reproduce valleys like Model 1 (*a* and *b*). In turn, mean topography correlates better than Models 1*a*–*b*. The W–E maximum swath profiles depict better

correlations than Models 1*a*–*b* across the whole study domain, i.e., from the orogenic area across the Andes to the west, and to the Atlantic coast to the east. It is important to note that our inversion model was designed to match two maximum elevation points, one in the Cordillera and another one across the foreland. The result of Model 2*a* illustrates a good match, not only in these two maximum points, but also in the remaining topography (Figs. 5c–d).

*4.4 Model 2b (Initial topography with an orogenic relief and long-wavelength uplift)*

The misfit for the best fitting free parameters was 4.4 (Fig. 6a). The $U_m$, k and Te were well constrained, with values of 0.2–1 mm/yr, 32–42 km and 2.0–4.0x $10^{-5}$ $m^{1-2m-1}$, respectively (see Supplementary Material Fig. S5). In turn, the inversion results show that the observed data are best explained using 0.27 mm/yr for $U_m$, 40 km for Te and 2.2 x $10^{-5}$ for k. With these value combinations, we computed a forward model using Fastscape. Figures 6b–d show these results and the relationships between observed and predicted thermochronological ages and maximum and mean topography across N–S and W–E swath profiles. In general, the thermochronological correlation of both systems was good, with an MSE of 4.1 (see Fig. 6b), similar to Model 2*a*. The swath profiles show similar correlations to Model 2*a* (see above, Figs. 6c–d).

## 5. Discussion

The inversion and forward landscape models allowed us to demonstrate that only a long-wavelength uplift geometry, from the Andes to the Atlantic coast, is needed to reproduce the Present-day topography. Initial topography (i.e., scenarios *a* and *b*) did not substantially affect our results when a long-wavelength uplift was considered (see Figs. 3–7). However, if we compare all the results in detail, we can identify some minor differences in the model which considers only local deformation and an initial relief across the Andes (Figs. 3–7).

Another important result from our study is that none of the models could accurately reproduce the thermochronological data. They are probably too simple to analyze ninety-two (92) cooling ages covering such a large area (800 x 700 kms). Thermochronological data are strongly influenced by local processes (see Georgieva et al., 2019), not considered in this contribution (e.g., local deformation, topography, erodibility or the presence of glaciers). For example, Georgieva et al., (2016, 2019) demonstrated that local fault displacements close to the present location of the CTJ satisfactorily explain the cooling ages of that region. In turn, for the same area, Andrić-Tomašević et al. (2021) referred to the occurrence of a subcrustal major thrust to account for cylindrical deformation geometry which would explain the distribution of low-temperature thermochronology ages. Guillaume et al. (2013) and Stevens Goddard and Fosdick (2019) interpreted the major late Miocene cooling event with exhumation after the ridge subduction, but only across the orogenic belt. In particular, Stevens Goddard and Fosdick (2019) estimated a time lag between the subduction time of different segments of the ridge and cooling ages. Given the lack of tectonic deformation in the last 12 Myr to account for thermochronology, they proposed the occurrence of a sort of "crustal welt" (or lower crustal thickening) across the Cordillera for ~160 km to generate uplift. Another important point to consider in future work, which might affect the matching between observed and modeled cooling ages, is the landscape model. It is possible that an algorithm that considers glacial erosion might improve part of the offsets.

Taking all this evidence into account, and considering the simplicity of the uplift and erosional functions (that do not consider glacial erosion) in our study (Figs. 3–7), we demonstrated that both Models 1 and 2 reproduce rather well the post 10 Myr exhumation history when the slab window started to affect the study region. The best fitting result for Model 1 provided high tectonic uplift rates in the last 12 Myr, around 2–3 mm/yr, when thrusting was minor to null, and a Te >60 km, which are values only found in pericratonic and

cratonic areas of South America (Pérez-Gussinyé et al., 2007). No geological and/or geophysical contributions have shown such high values in Patagonia. Model 2, in contrast, yielded more realistic quantities. While the uplift rate ($U_m$) in the last 12 Myr is 0.3 mm/yr, similar to those proposed by Pedoja et al. (2011) for the Atlantic coast, Te = 34–40 km is consistent with values estimated by Álvarez et al. (2016) for the study region using gravity inversion. This demonstrates that in order to explain the regional topographic observations and cooling ages, a long-wavelength uplift or rebound would adjust better than a localized orogenic uplift, only across the Cordillera.

Since the 1990s, the formation of slab windows in Patagonia has mainly been mentioned (Gorring et al., 1997; Ramos and Kay, 1992) to account for basalt formation. However, only a few studies have dealt with the connection to long-wavelength uplift (Guillaume et al., 2009; 2013). These contributions investigated the impact of the associated mantle flow on vertical surface motion during the Neogene. They concluded that the episodic northward opening of a slab window below southern Patagonia (Breitsprecher and Thorkelson, 2009) would have canceled the dynamic downward deflection of the continental plate above the subduction zone, inducing a dynamic rebound or uplift (i.e., the cessation of the dynamic deflection) of the overriding plate. An alternative hypothesis was more recently suggested by Ávila and Dávila (2020), who calculated residual topography and isostatic uplift across the Patagonian foreland from the early–middle Miocene to the Present day (when the slab window formation began to migrate northward to its current position). These authors proposed that isostatic uplift by lithospheric thinning produced by a heat flow increase during the formation of the slab window (Ávila and Dávila, 2018) would have been the main driving mechanism for generating the long-wavelength topography (Ávila and Dávila, 2020). However, they did not disregard the hypothesis that dynamic uplift could have played a minor role in topography overlapping the isostatic rebound effect. Although our contribution supports a large-scale

process, covering Patagonia from coast to coast, it cannot differentiate between dynamic uplift and lithospheric rebound by thinning. Some works have mentioned that both processes could have partly overlapped (Ávila and Dávila, 2020; Flament et al., 2015; Guillaume et al., 2009), although asthenospheric and lithospheric mantle processes would have had different timings. While dynamic uplift is an instantaneous process (Hager and O´Connel, 1981), generated by a change in subduction conditions (the "passive" dynamic uplift of Guillaume et al., 2013) or a real upwelling driven by a mantle flow (the "active" dynamic uplift of Guillaume et al., 2013), a lithospheric rebound would require reduction of the lithospheric thickness by degradation of the lithospheric mantle.

As discussed previously, a change in subduction conditions represents the most plausible scenario. It is questionable whether the lithospheric thinning process would account for the uplift observations, given that different studies have shown that it might take ~10 Myr to occur (Heyn and Conrad, 2022). Nevertheless, it is known that Patagonia was affected by older thermal anomaly events (e.g., Aragón et al., 2013) that might have degraded the lithospheric mantle before the Miocene slab window formation and, consequently, facilitated and accelerated a lithospheric removal, followed by thinning and rebound. This interpretation would be in line with a recent tomography in southern Patagonia by Mark et al. (2022), who presented the first seismic velocity model covering the slab window area. They proposed the occurrence of a slow velocity anomaly in the uppermost mantle, which suggests warm temperatures, low viscosity, and possibly partial melting. The latter, in turn, suggests that the lithospheric mantle could have been thermally eroded in the areas surrounding the CTJ, over the youngest part of the slab window (Fig. 1a). Our model supports the idea that both dynamic uplift and lithospheric mantle processes are valid and complementary hypotheses for explaining the current topography and reproducing the youngest cooling ages in southern Patagonia.

## 6. Conclusions

By combining inverse and forward landscape evolution models to match modeled and observed low-temperature thermochronological ages and Present-day topography, this contribution has demonstrated that only a long-wavelength uplift, spanning Patagonia from coast to coast, can reproduce the data set. The parameters constrained by inversion, i.e., erosion efficiency, rock uplift rates, and effective elastic thickness, show reasonable values (and are consistent with other geophysical data), when the models use long-wavelength uplifts. Two likely large-scale processes might explain these results in southern Patagonia, associated with subcrustal mechanisms in the lithospheric or/and asthenospheric mantle: lithospheric thinning (Ávila and Dávila, 2020) or dynamic topography (Guillaume et al., 2009), respectively. These driving forces, likely interrelated (Ávila and Dávila, 2020), would have been the main drivers for the topographic changes and exhumation reported since the arrival of the oceanic ridge at the subduction zone and the formation of the asthenospheric window from the middle–late Miocene to the Present day. For this long-wavelength-driven case, our best model choice, the uplift rate was 0.3 mm/yr, similar to the rates proposed by Pedoja et al., (2011) for the Atlantic coast, and the effective elastic thickness was 34 km, consistent with values estimated by Álvarez et al., (2016). We do not rule out the possibility that more local tectonic forces may have interfered in some sectors with the long-wavelength upwelling, favoring a better fit between models and observations.

## 7. Acknowledgements

We thank Samuel Angiboust, Nicolas Flament and an anonymous reviewer for their valuable and constructive suggestions and reviews. We appreciate Argentine funding from FONCyT (PICT 2018), UNC (SECyT 2018) and CONICET (PIP2020).

## 8. References

Álvarez, O., Klinger, F.L., Giménez, M., Ruiz, F., Martinez, P., 2016. Density and thermal structure of the Southern Andes and adjacent foreland from 32 to 55 S using Earth gravity field models, in: Growth of the Southern Andes. Springer, pp. 9–31.

Andrić-Tomašević, N., Falkowski, S., Georgieva, V., Glotzbach, C., Strecker, M.R., Ehlers, T.A., 2021. Quantifying Tectonic and Glacial Controls on Topography in the Patagonian Andes (46.5°S) From Integrated Thermochronometry and Thermo-Kinematic Modeling. J. Geophys. Res. Earth Surf. 126, e2020JF005993. https://doi.org/10.1029/2020JF005993

Aragón, E., Pinotti, L., D'Eramo, F., Castro, A., Rabbia, O., Coniglio, J., Demartis, M., Hernando, I., Cavarozzi, C.E., Aguilera, Y.E., 2013. The Farallon-Aluk ridge collision with South America: Implications for the geochemical changes of slab window magmas from fore- to back-arc. Geosci. Front. 4, 377–388. https://doi.org/10.1016/j.gsf.2012.12.004

Aramendía, I., JI., C., Ghiglione, M., Bouza P, J., 2022. Timing and stratigraphic evolution of a Miocene foreland unroofing sequence in the Austral-Magallanes Basin during Southern Patagonian Andes uplift. J. Geol. Soc. London. 0, jgs2022-038. https://doi.org/10.1144/jgs2022-038

Ávila, P., Dávila, F.M., 2020. Lithospheric thinning and dynamic uplift effects during slab window formation, southern Patagonia (45˚-55˚ S). J. Geodyn. 133, 101689. https://doi.org/10.1016/J.JOG.2019.101689

Ávila, P., Dávila, F.M., 2018. Heat flow and lithospheric thickness analysis in the Patagonian asthenospheric windows, southern South America. Tectonophysics 747–748, 99–107. https://doi.org/10.1016/J.TECTO.2018.10.006

Blisniuk, P.M., Stern, L.A., Chamberlain, C.P., Idleman, B., Zeitler, P.K., 2005. Climatic and ecologic changes during Miocene surface uplift in the Southern Patagonian Andes. Earth

Planet. Sci. Lett. 230, 125–142. https://doi.org/10.1016/j.epsl.2004.11.015

Braun, J., der Beek, P., Batt, G., 2006. Quantitative thermochronology: numerical methods for the interpretation of thermochronological data. Cambridge University Press.

Braun, J., Willett, S.D., 2013. A very efficient O(n), implicit and parallel method to solve the stream power equation governing fluvial incision and landscape evolution. Geomorphology 180–181, 170–179. https://doi.org/10.1016/j.geomorph.2012.10.008

Braun, J., Zwartz, D., Tomkin, J.H. 1999. A new surface-processes model combining glacial and fluvial erosion. Annals of Glaciology 28, 282-290.

Breitsprecher, K., Thorkelson, D.J., 2009. Neogene kinematic history of Nazca-Antarctic-Phoenix slab windows beneath Patagonia and the Antarctic Peninsula. Tectonophysics 464, 10–20. https://doi.org/10.1016/j.tecto.2008.02.013

Christeleit, E.C., Brandon, M.T., Shuster, D.L., 2017. Miocene development of alpine glacial relief in the Patagonian Andes, as revealed by low-temperature thermochronometry. Earth Planet. Sci. Lett. 460, 152–163. https://doi.org/10.1016/j.epsl.2016.12.019

Coronato, A., Rabassa, J., 2011. Chapter 51 - Pleistocene Glaciations in Southern Patagonia and Tierra del Fuego, in: Ehlers, J., Gibbard, P.L., Hughes, P.D.B.T.-D. in Q.S. (Eds.), Quaternary Glaciations - Extent and Chronology. Elsevier, pp. 715–727. https://doi.org/10.1016/B978-0-444-53447-7.00051-9

Croissant, T., Braun, J., 2014. Constraining the stream power law: A novel approach combining a landscape evolution model and an inversion method. Earth Surf. Dyn. 2, 155–166. https://doi.org/10.5194/esurf-2-155-2014

Cuitiño, J.I., Fernicola, J.C., Kohn, M.J., Trayler, R., Naipauer, M., Bargo, M.S., Kay, R.F., Vizcaíno, S.F., 2016. U-Pb geochronology of the Santa Cruz Formation (early Miocene) at the Río Bote and Río Santa Cruz (southernmost Patagonia, Argentina): Implications for the correlation of fossil vertebrate localities. J. South Am. Earth Sci. 70, 198–210.

https://doi.org/10.1016/j.jsames.2016.05.007

Cuitiño, J.I., Pimentel, M.M., Ventura Santos, R., Scasso, R.A., 2012. High resolution isotopic ages for the early Miocene "Patagoniense" transgression in Southwest Patagonia: Stratigraphic implications. J. South Am. Earth Sci. 38, 110–122. https://doi.org/10.1016/j.jsames.2012.06.008

Curie, C.A., Hyndman, R.D., 2006. The thermal structure of subduction zone back arcs. J. Geophys. Res. Solid Earth 111, 1–22. https://doi.org/10.1029/2005JB004024

Flament, N., Gurnis, M., Müller, R. D., Bower, D. J., Husson, L. 2015. Influence of subduction history on South American topography. Earth and Planetary Science Letters, 430, 9-18.

Flynn, J.J., Swisher, C.C., 1995. Cenozoic South American land mammal ages: correlation to global geochronologies.

Fosdick, J.C., Grove, M., Hourigan, J.K., Calderón, M., 2013. Retroarc deformation and exhumation near the end of the Andes, southern Patagonia. Earth Planet. Sci. Lett. 361, 504–517. https://doi.org/10.1016/j.epsl.2012.12.007

Furlong, K.P., Govers, R., 1999. Ephemeral crustal thickening at a triple junction: The Mendocino crustal conveyor. Geology 27, 127–130.

Georgieva, V., Gallagher, K., Sobczyk, A., Sobel, E.R., Schildgen, T.F., Ehlers, T.A., Strecker, M.R., 2019. Effects of slab-window, alkaline volcanism, and glaciation on thermochronometer cooling histories, Patagonian Andes. Earth Planet. Sci. Lett. 511, 164–176.

Georgieva, V., Melnick, D., Schildgen, T.F., Ehlers, T.A., Lagabrielle, Y., Enkelmann, E., Strecker, M.R., 2016. Tectonic control on rock uplift, exhumation, and topography above an oceanic ridge collision: Southern Patagonian Andes (47°S), Chile. Tectonics 35, 1317–1341. https://doi.org/10.1002/2016TC004120

Ghiglione, M.C., Ramos, V.A., Cuitiño, J., Barberón, V., 2016. Growth of the Southern

Patagonian Andes (46–53°S) and Their Relation to Subduction Processes BT - Growth of the Southern Andes, in: Folguera, A., Naipauer, M., Sagripanti, L., C. Ghiglione, M., Orts, D.L., Giambiagi, L. (Eds.). Springer International Publishing, Cham, pp. 201–240. https://doi.org/10.1007/978-3-319-23060-3_10

Gianni, G.M., Pesce, A., Soler, S.R., 2018. Transient plate contraction between two simultaneous slab windows: Insights from Paleogene tectonics of the Patagonian Andes. J. Geodyn. 121, 64–75. https://doi.org/https://doi.org/10.1016/j.jog.2018.07.008

Gorring, M., Kay, S.M., Zeitler, P.K., Ramos, V.A., Rubiolo, D., Fernandez, M.I., Panza, J.L., 1997. Neogene Patagonian plateau lavas: Continental magmas associated with ridge collision at the Chile Triple Junction. Tectonics 16, 1. https://doi.org/10.1029/96TC03368

Groome, W.G., Thorkelson, D.J., 2009. The three-dimensional thermo-mechanical signature of ridge subduction and slab window migration. Tectonophysics 464, 70–83. https://doi.org/10.1016/j.tecto.2008.07.003

Guillaume, B., Gautheron, C., Simon-Labric, T., Martinod, J., Roddaz, M., Douville, E., 2013. Dynamic topography control on Patagonian relief evolution as inferred from low temperature thermochronology. Earth Planet. Sci. Lett. 364, 157–167. https://doi.org/10.1016/j.epsl.2012.12.036

Guillaume, B., Martinod, J., Husson, L., Roddaz, M., Riquelme, R., 2009. Neogene uplift of central eastern Patagonia: Dynamic response to active spreading ridge subduction? Tectonics 28, 1–19. https://doi.org/10.1029/2008TC002324

Guivel, C., Morata, D., Pelleter, E., Espinoza, F., Maury, R.C., Lagabrielle, Y., Polvé, M., Bellon, H., Cotten, J., Benoit, M., Suárez, M., de la Cruz, R., 2006. Miocene to Late Quaternary Patagonian basalts (46-47°S): Geochronometric and geochemical evidence for slab tearing due to active spreading ridge subduction. J. Volcanol. Geotherm. Res. 149, 346–370. https://doi.org/10.1016/j.jvolgeores.2005.09.002

Haeussler, P.J., Bradley, D.C., Wells, R.E., Miller, M.L., 2003. Life and death of the Resurrection plate: Evidence for its existence and subduction in the northeastern Pacific in Paleocene–Eocene time. GSA Bull. 115, 867–880. https://doi.org/10.1130/0016-7606(2003)115<0867:LADOTR>2.0.CO;2

Hager, B.H., O'Connell, R.J. 1981. A simple global model of plate dynamics and mantle convection. Journal of Geophysical Research: Solid Earth 86(B6), 4843-4867.

Haschke, M., Sobel, E.R., Blisniuk, P.M., Strecker, M.R., Warkus, F., 2006. Continental response to active ridge subduction. Geophys. Res. Lett. 33, 1–5. https://doi.org/10.1029/2006GL025972

Hergarten, S., 2021. Modeling glacial and fluvial landform evolution at large scales using a stream-power approach, Earth Surf. Dynam. 9, 937-952.

Herman, F., Brandon, M. 2015. Mid-latitude glacial erosion hotspot related to equatorial shifts in southern Westerlies. Geology 43(11), 987-990.

Heyn, B.H., Conrad, C.P., 2022. On the Relation Between Basal Erosion of the Lithosphere and Surface Heat Flux for Continental Plume Tracks. Geophys. Res. Lett. 49, e2022GL098003. https://doi.org/10.1029/2022GL098003

Husson, L., Guillaume, B., Martinod, J., 2019. Multichronometer thermochronologic modeling of migrating spreading ridge subduction in southern Patagonia: COMMENT. Geology 47(10), e483-e483.

Lagabrielle, Y., Suárez, M., Malavieille, J., Morata, D., Espinoza, F., Maury, R.C., Scalabrino, B., Barbero, L., Cruz, R. de la, Rossello, E., Bellon, H., 2007. Pliocene extensional tectonics in the Eastern Central Patagonian Cordillera: geochronological constraints and new field evidence. Terra Nov. 19, 413–424. https://doi.org/10.1111/j.1365-3121.2007.00766.x

Mark, H.F., Wiens, D.A., Ivins, E.R., Richter, A., Ben Mansour, W., Magnani, M.B.,

Marderwald, E., Adaros, R., Barrientos, S., 2022. Lithospheric Erosion in the Patagonian Slab Window, and Implications for Glacial Isostasy. Geophys. Res. Lett. 49, e2021GL096863. https://doi.org/10.1029/2021GL096863

Martina, F., Ávila, P., Dávila, F.M., Parra, M., 2020. Triassic-Jurassic thermal evolution and exhumation of the western Gondwana foreland: Thermochronology and basalt thermobarometry from the Argentine Sierras Pampeanas. J. South Am. Earth Sci. https://doi.org/10.1016/j.jsames.2020.102956

Mercer, J.H., Sutter, J.F., 1982. Late Miocene—earliest Pliocene glaciation in southern Argentina: implications for global ice-sheet history. Palaeogeogr. Palaeoclimatol. Palaeoecol. 38, 185–206. https://doi.org/10.1016/0031-0182(82)90003-7

Parras, A., Cuitiño, J.I., 2021. Revised chrono and lithostratigraphy for the Oligocene-Miocene Patagoniense marine deposits in Patagonia: Implications for stratigraphic cycles, paleogeography, and major drivers. J. South Am. Earth Sci. 110, 103327. https://doi.org/10.1016/j.jsames.2021.103327

Pascual, R., Jaureguizar, E.O., 1990. Evolving climates and mammal faunas in cenozoic South America. J. Hum. Evol. 19, 23–60. https://doi.org/10.1016/0047-2484(90)90011-Y

Pedoja, K., Regard, V., Husson, L., Martinod, J., Guillaume, B., Fucks, E., Iglesias, M., Weill, P., 2011. Uplift of quaternary shorelines in eastern Patagonia: Darwin revisited. Geomorphology 127, 121–142. https://doi.org/10.1016/j.geomorph.2010.08.003

Pérez-Gussinyé, M., Lowry, A.R., Watts, A.B., 2007. Effective elastic thickness of South America and its implications for intracontinental deformation. Geochemistry, Geophys. Geosystems 8. https://doi.org/10.1029/2006GC001511

Rabassa, J., Coronato, A., 2002. Glaciaciones del Cenozoico tardío. Geol. y Recur. Nat. St. Cruz 303–315.

Ramos, V.A., Kay, S.M., 1992. Southern Patagonian plateau basalts and deformation: Backarc

testimony of ridge collisions. Tectonophysics 205, 261–282. https://doi.org/10.1016/0040-1951(92)90430-E

Russo, R.M., VanDecar, J.C., Comte, D., Mocanu, V.I., Gallego, A., Murdie, R.E., 2010. Subduction of the Chile Ridge: Upper mantle structure and flow. GSA Today 20, 4–10. https://doi.org/10.1130/GSATG61A.1

Sambridge, M., 1999. Geophysical inversion with a neighbourhood algorithm—I. Searching a parameter space. Geophys. J. Int. 138, 479–494. https://doi.org/10.1046/j.1365-246X.1999.00876.x

Scalabrino, B., Lagabrielle, Y., Malavieille, J., Dominguez, S., Melnick, D., Espinoza, F., Suarez, M., Rossello, E., 2010. A morphotectonic analysis of central Patagonian Cordillera: Negative inversion of the Andean belt over a buried spreading center? Tectonics 29. https://doi.org/10.1029/2009TC002453

Stevens Goddard, A.L., Fosdick, J.C., 2019. Multichronometer thermochronologic modeling of migrating spreading ridge subduction in southern Patagonia. Geology 47, 555–558.

Suárez, R., Sue, C., Ghiglione, M., Guillaume, B., Ramos, M., Martinod, J., Barberón, V., 2021. Seismotectonic implications of the South Chile ridge subduction beneath the Patagonian Andes. Terra Nov. 33, 364–374. https://doi.org/https://doi.org/10.1111/ter.12521

Thomson, S.N., Brandon, M.T., Tomkin, J.H., Reiners, P.W., Vásquez, C., Wilson, N.J., 2010. Glaciation as a destructive and constructive control on mountain building. Nature 467, 313–317. https://doi.org/10.1038/nature09365

Thorkelson, D.J., 1996. Subduction of diverging plates and the principles of slab window formation. Tectonophysics 255, 47–63. https://doi.org/10.1016/0040-1951(95)00106-9

Thorkelson, D.J., Madsen, J.K., Sluggett, C.L., 2011. Mantle flow through the Northern Cordilleran slab window revealed by volcanic geochemistry. Geology 39, 267–270.

Turcotte, D.L., Schubert, G., 2002. Geodynamics. Cambridge university press.

Underwood, M.B., 1993. Thermal evolution of the Tertiary Shimanto Belt, Southwest Japan: An example of ridge-trench interaction. Geological Society of America.

Whipple, K.X., Tucker, G.E., 1999. Dynamics of the stream-power river incision model: Implications for height limits of mountain ranges, landscape response timescales, and research needs. J. Geophys. Res. Solid Earth 104, 17661–17674. https://doi.org/10.1029/1999JB900120

Willett, C.D., Ma, K.F., Brandon, M.T., Hourigan, J.K., Christeleit, E.C., Shuster, D.L., 2020. Transient glacial incision in the Patagonian Andes from ~6 Ma to present. Sci. Adv. https://doi.org/10.1126/sciadv.aay1641

## 9. Figure captions

**Figure 1 a)** Map of southern Patagonia showing topography, location of thermochronological ages and the main stratigraphic and tectonic features referenced in our work. The Andean thrust fronts (easternmost deformation) are represented as a solid black line with black triangles. The belt between the trench (solid lines with circles indicate the tracking of the migration of the Chile Triple Junction, CTJ) and the thrust front is the orogenic area (Patagonian Andes). The extent of the Patagonian slab window is shown with thick, solid black lines. The Oligocene-lower Miocene marine beds are shown as orange polygons. AFT samples are illustrated as magenta dots, and AHe samples as yellow dots. The white rectangle shows the position of the study domain and E–W and N–S swath profile represented in Figure 1b. CTJ: Chile Triple Junction (After Breitsprecher and Thorkelson, 2009). FTS: Fagnano transform system. **b)** E–W swath profile showing the maximum topography across the white rectangle shown in Figure 1a. Black points indicate the observed topography used. The comparison between modeled and

observed topography was made using the maximum modeled topography from 100–400 km to compare with the 3200 m point and from 400–700 km to compare with 800 m.

**Figure 2.** Parametrization for Models 1 and 2, and scenarios *a* and *b*. **a)** Schematic initial topography and precipitation for Scenario *a*. Note the precipitation rates used in the models were 1500 mm/yr between 20 and 16.5 Myr, and from 16.5 to 0 Myr (since the formation of the rain shadow), 3000 mm/yr to the left boundary (Andes) and 200 mm/yr to the right (i.e., towards the Patagonian foreland: $P = 3e^{\left(\frac{-1(y-150000)}{120000}\right)^2} + 2$). **b)** Schematic initial topography and precipitation for Scenario *b*. Initial topography started with 2000 m high across the cordillera region and flat in the foreland. Precipitation rate was 3000 mm/yr to the left boundary (Andes) and 200 mm/yr to the right (i.e., toward the Patagonian foreland). **c)** Schematic uplift rate geometry used in Model 1. Between 20 and 12 Myr, the $U_{t1}$ is the maximum tectonic uplift (crustal shortening), represented by the maximum height of the triangle. Between 12 ($t_1$) and 0 Ma, the uplift rate decreases as the slab window migrates northward. The arrow indicates the direction of slab window migration. $t_1$; $t_{i-1}$; ti refers to time passing. **d)** Schematic uplift rate geometry for Model 2. Between 20 and 12 Myr, $U_{t2}$ is the maximum tectonic uplift (crustal shortening), represented by the maximum height of the triangle. Uplift rate geometry for Model 2 between 12 ($t_1$) and 0 Myr is represented by a Gaussian-type function ($U = U_m e^{\left(\frac{-2(y-0{,}075t)}{150000}\right)^2}$), Um decreases linearly from west to east with a slope of 0.8. The arrow indicates the direction of slab window migration. $t_1$; t i-1; ti refers to time passing.

**Figure 3.** Results of the NA inversion for Model 1*a*. a) Scatter plots colored by misfit values for pairs of free parameters in Inversion 1*a*: Erosion efficiency (k), effective elastic thickness (Te), and tectonic uplift rate from 12 to 0 M Myr ($U_{t1}$). The run with the smallest misfit is indicated with a red star. b) Comparison between modeled and observed cooling ages (AFT,

dark gray circles, and AHe, light gray triangles) predicted by the best-fit analysis. **c)** Comparison between modeled (red) and observed (gray) for maximum (solid) and mean (dashed) topography plotted as a N–S profile of the study region. d) Comparison between modeled (red) and observed (gray) for maximum (solid) and mean (dashed) topography plotted as a W–E profile of the study region.

**Figure 4.** Results of the NA inversion for Model 1*b*. See other details and captions in Figure 3.

**Figure 5.** Results of the NA inversion for Model 2*a*. **a)** Scatter plots colored by misfit values for pairs of free parameters in Inversion 1*a*: Erosion efficiency (k), effective elastic thickness (Te), and tectonic uplift rate from 12 to 0 Myr ($U_m$). The run with the smallest misfit is indicated with a red star. b) Comparison between modeled and observed cooling ages (AFT, dark gray circles, and AHe, light gray triangles) predicted by the best-fit analysis. **c)** Comparison between modeled (red) and observed (gray) for maximum (solid) and mean (dashed) topography plotted as a N–S profile of the study region. d) Comparison between modeled (red) and observed (gray) for maximum (solid) and mean (dashed) topography plotted as a W–E profile of the study region.

**Figure 6.** Results of the NA inversion for Model 2*b*. See other details and captions in Figure 5.

**Figure 7.** Simplified topographic profiles (from Fig. 3d, Fig. 4d, Fig. 5d, Fig. 6d) showing the influences of **(a)** medium (crustal tectonics) versus **(b)** long (mantle-driven) wavelength forces on topography across the entire Patagonia, from the Pacific to the Atlantic coasts. Note that

even though the modeled cooling ages along the orogen reproduced the observed ages rather well (see Figs. 4b and 6b), without large-scale controls, the observed and modeled topographies across the foreland and the Patagonian Atlantic coast do not match. The position of the thrust front is strikingly far from the high reliefs reported in the foreland.

## Figures

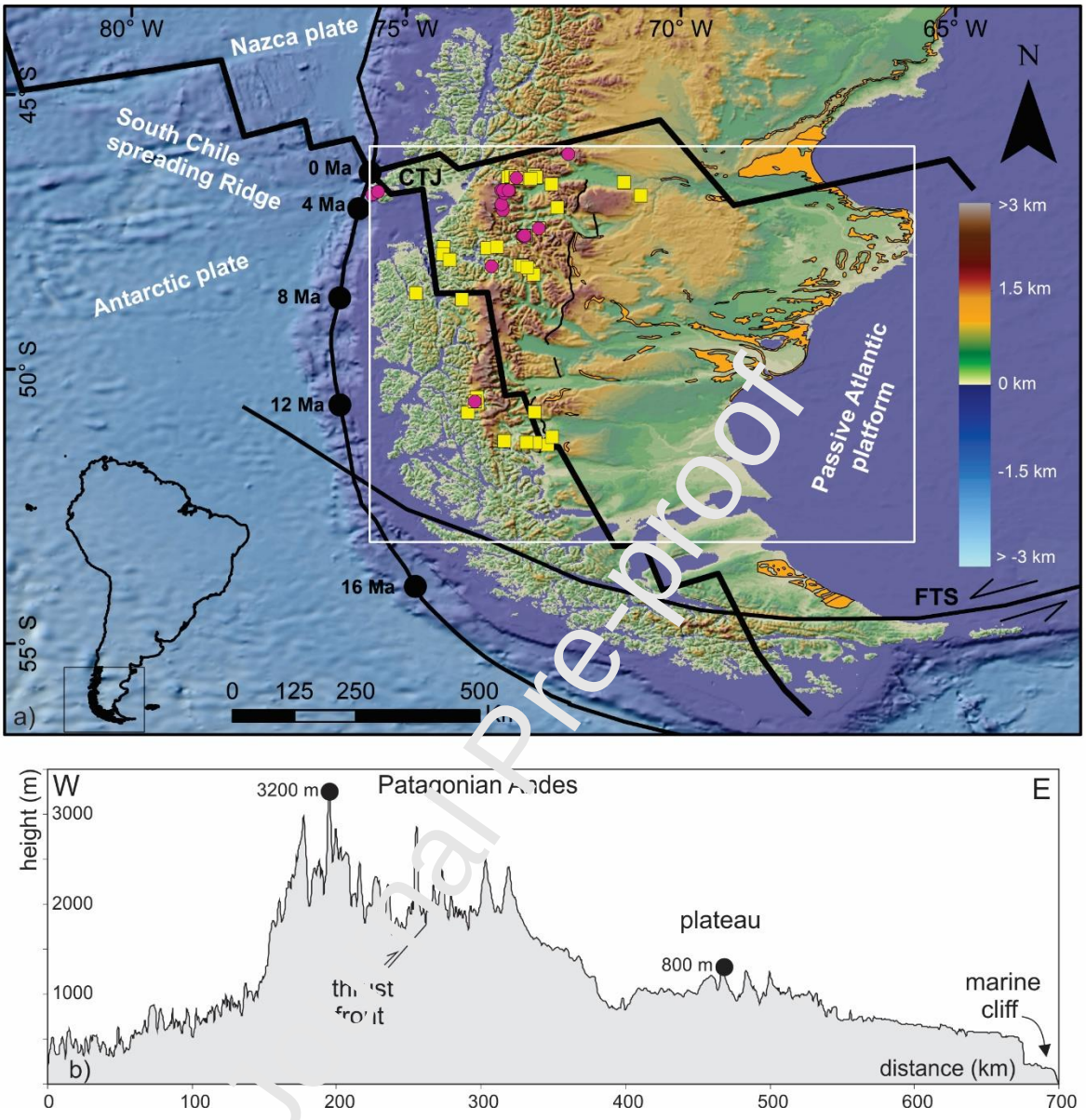


*Figure 1*

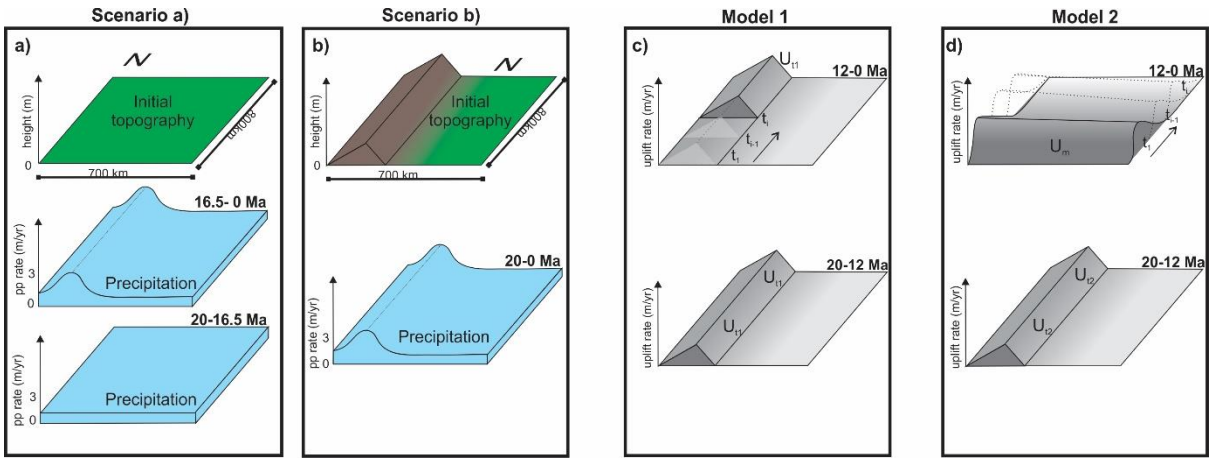


*Figure 2*

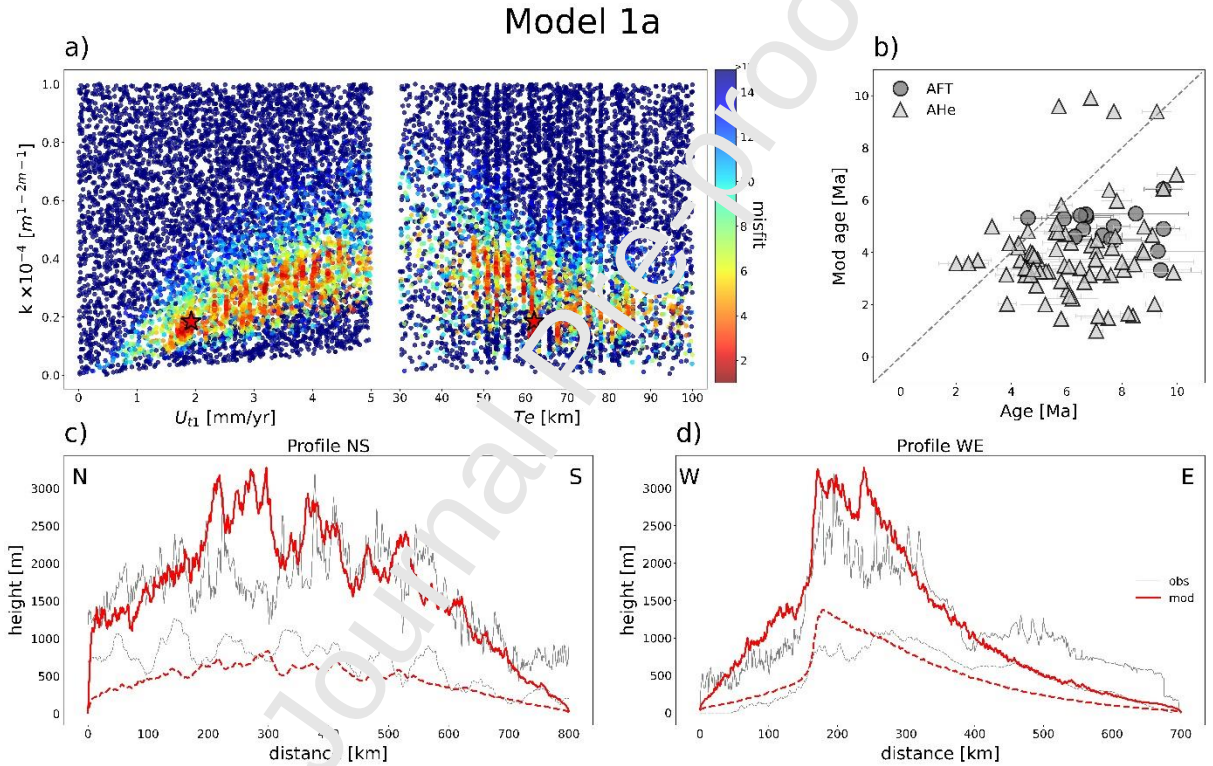


*Figure 3*

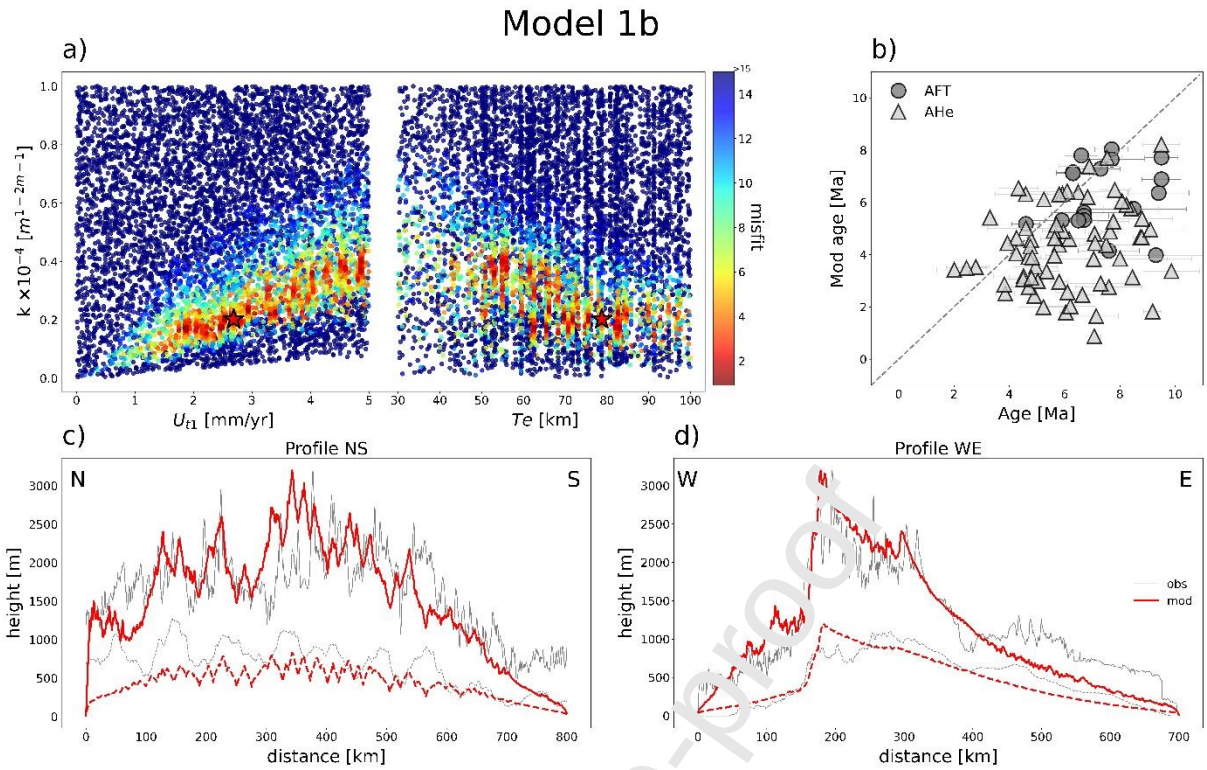


*Figure 4*

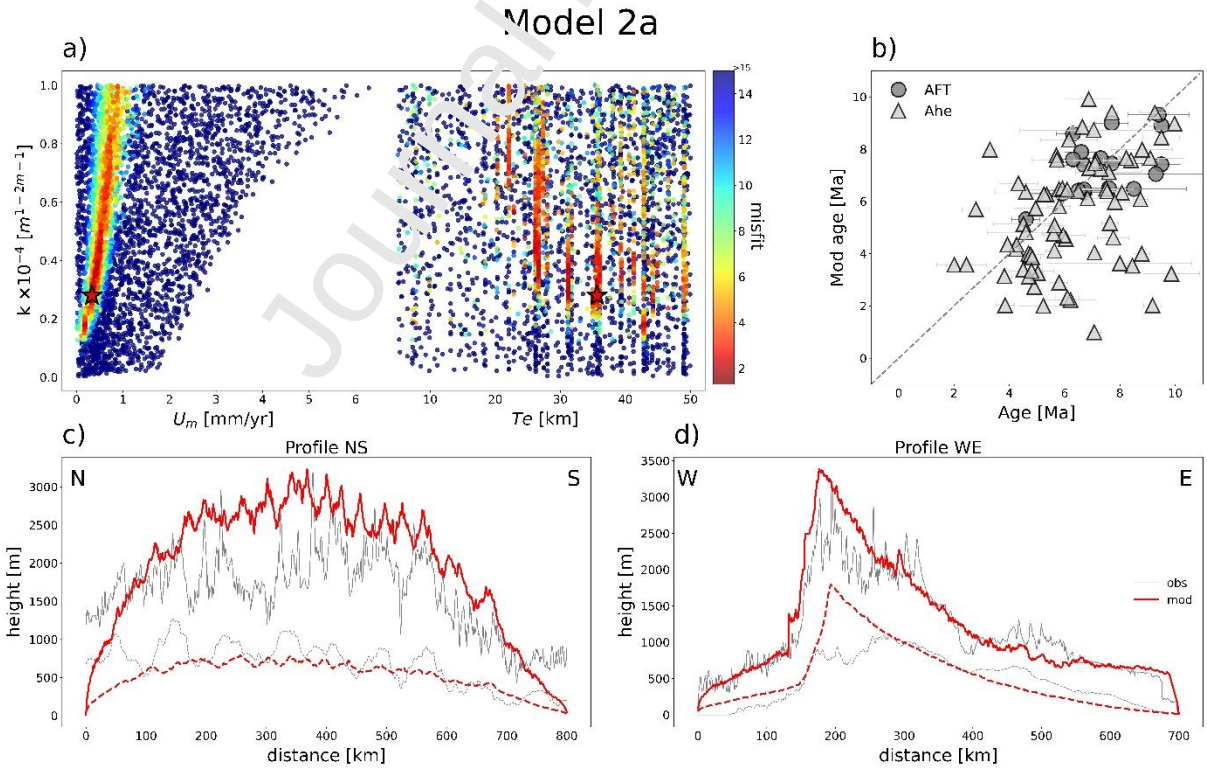


*Figure 5*

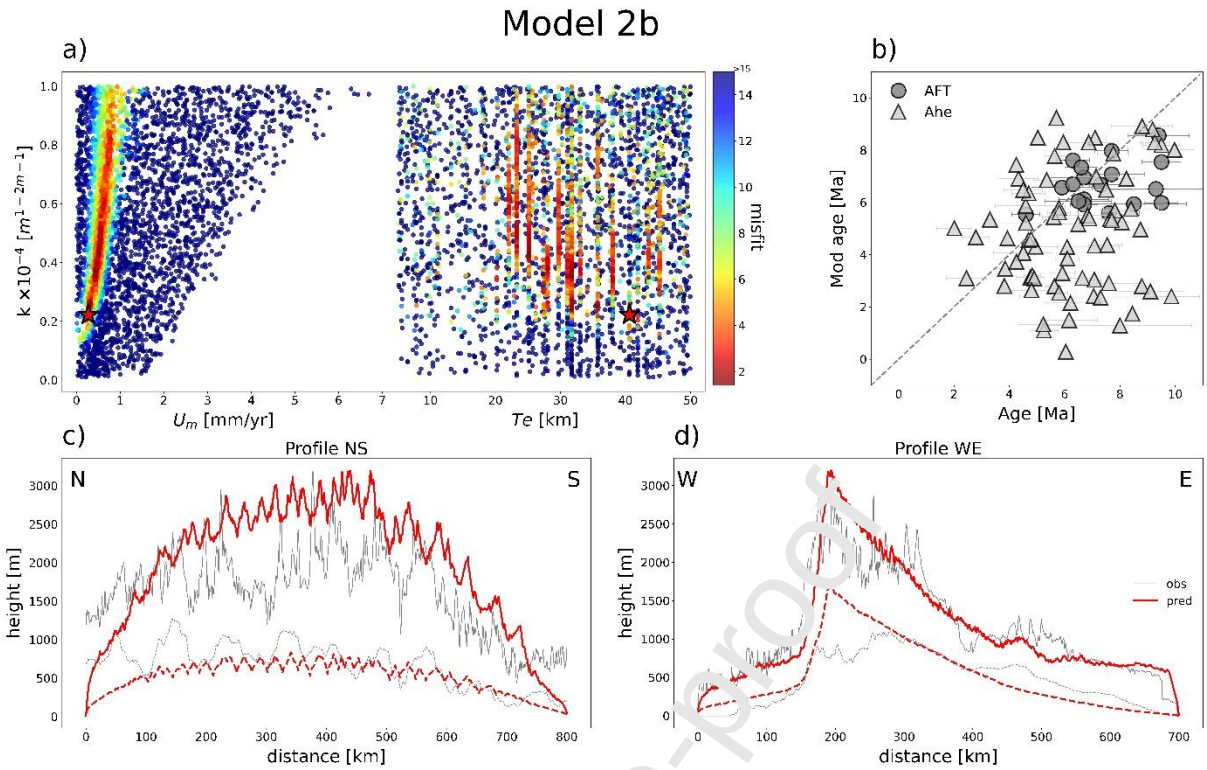


*Figure 6*

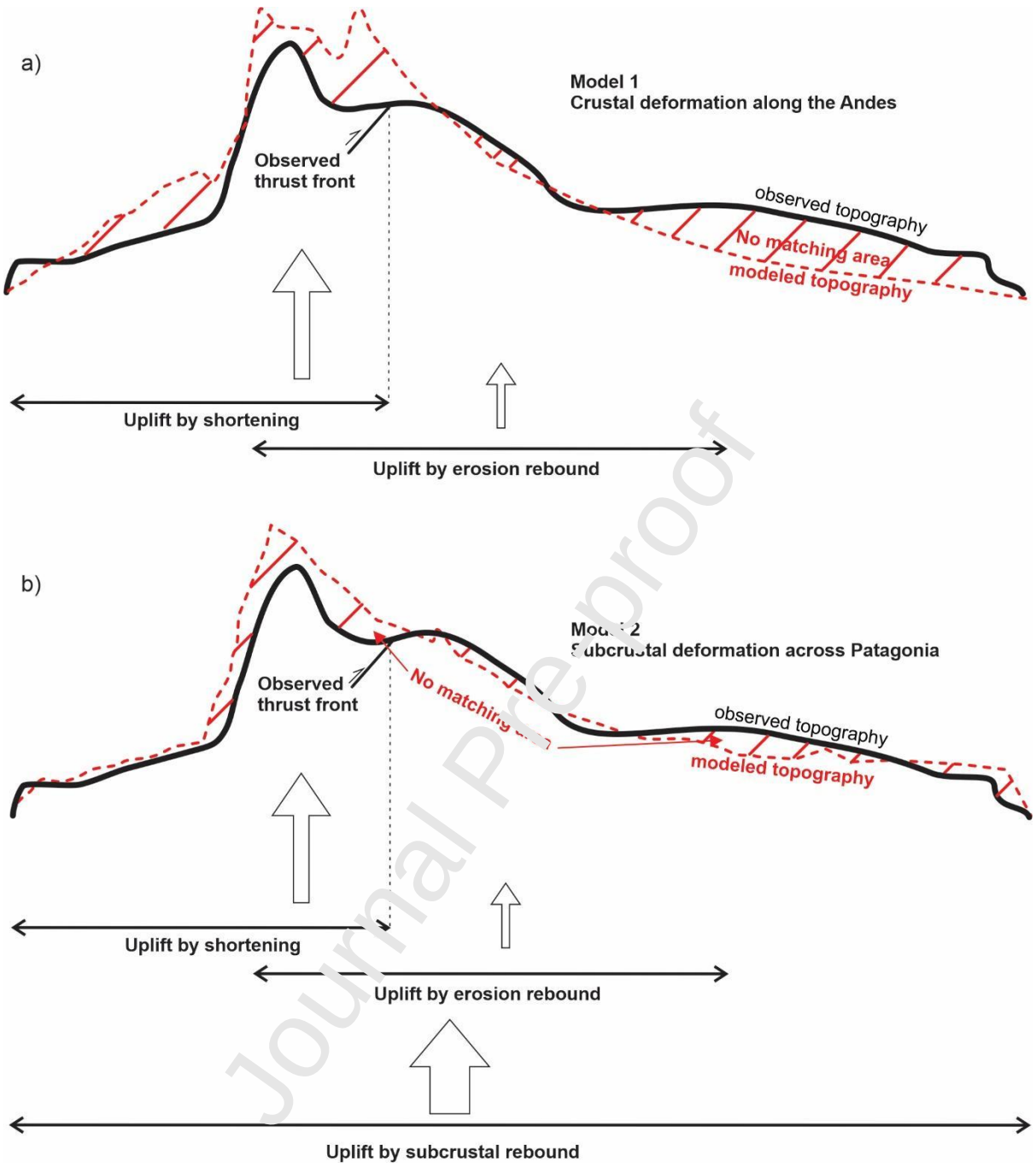




*Figure 7*

**Ávila Pilar:** Conceptualization, Methodology, Formal analysis, Investigation, Resources, Data Curation, Writing - Original Draft, Writing - Review & Editing, Visualization

**Ávila Milagros:** Conceptualization, Methodology, Software, Validation, Formal analysis, Visualization

**Dávila Federico:** Conceptualization, Writing - Original Draft, Writing - Review & Editing, Visualization, Supervision, Project administration, Funding acquisition

**Ezpeleta Miguel:** Conceptualization, Writing - Original Draft, Writing - Review & Editing

**Castellano Nesvit E.:** Conceptualization, Methodology, Formal analysis, Investigation

**Declaration of interests**

☒The authors declare that they have no known competing financial interests or personal relationships that could have appeared to influence the work reported in this paper.

☐The authors declare the following financial interests/personal relationships which may be considered as potential competing interests:

**Highlights**

1. Southern Patagonia records rock uplift and plateau formation from Miocene-Present
2. Long-wavelength uplift geometry is required for reproducing Present-day topography
3. Long-wavelength uplift geometry is useful for reproducing Present-day cooling ages
4. A slab window is responsible for long-wavelength uplift in southern Patagonia